Electronic structure of the deep boron acceptor in boron-doped 6*H*-SiC

A. v. Duijn-Arnold
Centre for the Study of the Excited States of Molecules, Leiden University, Leiden, The Netherlands

T. Ikoma
Institute for Chemical Reaction Science, Tohoku University, Katahira 2-1-1, Aobaku, Sendai 980-77, Japan

O. G. Poluektov
Institute of Chemical Physics, Russian Academy of Sciences, Moscow, Russia

P. G. Baranov and E. N. Mokhov
A. F. Ioffe Physico-Technical Institute, St. Petersburg, Russia

J. Schmidt
Centre for the Study of the Excited States of Molecules, Leiden University, Leiden, The Netherlands
(Received 9 July 1997)

A high-frequency (95 GHz) and conventional-frequency (9.3 GHz) pulsed electron paramagnetic resonance and electron-nuclear double resonance (ENDOR) study is reported on the deep boron acceptor in 6*H*-SiC. The results support a model in which the deep boron acceptor consists of a boron on a silicon position with an adjacent carbon vacancy. The carbon vacancy combines with a boron along the hexagonal *c* axis. It is concluded that 70–90 % of the spin density resides in the silicon dangling bonds surrounding the vacancy and another 9% on the neighboring carbon atoms. The spin-density distribution is more localized than in the case of the shallow boron acceptor as deduced from the ENDOR experiments. [S0163-1829(98)01003-0]

I. INTRODUCTION

Silicon carbide is a wide band-gap semiconductor material that has considerable potential for high-temperature, high-power, and high-frequency electronic applications. The most important acceptor impurities in SiC are B, Al, and Ga. These impurities can be introduced during the growth or afterwards by diffusion or implantation. A substitutional atom of a group-III element normally acts as an acceptor in SiC since there is a deficit of one valence electron to complete the normal tetrahedral bonding. At sufficiently low temperatures, the hole is localized near the acceptor atom, at high temperatures, it ionizes and gives rise to *p*-type conduction.

The group-III element acceptors in SiC have been studied using Hall effect, deep-level transient spectroscopy (DLTS), and optical spectroscopy.[1] It was discovered that B creates a shallow as well as a deep acceptor level. The shallow B center (sB) with an activation energy of 0.30–0.39 eV was observed in Hall-effect studies and admittance spectroscopy measurements. The deep B center (dB) was first detected by photoluminescence measurements.[2,3] It was suggested that the characteristic high-temperature bright-yellow luminescence in B-doped 6*H*-SiC is due to recombination involving the dB center on the one hand and N donors and conduction electrons on the other hand.[2] Based on this suggestion the ionization energy of the dB center was estimated to be more than 0.65 eV. DLTS investigations[4,5] and capacitance methods[6] also point to the presence of a deep and shallow boron acceptor level. The activation energies were estimated to be between 0.22 and 0.35 eV for sB and between 0.55 and 0.75 eV for dB.

For Al and Ga one would expect a similar behavior as for B. Indeed, the incorporation of Al in 6*H*-SiC introduces shallow acceptor levels at $E_v+0.239$ eV for the hexagonal site (h) and $E_v+0.248$ eV for the quasicubic sites (k_1,k_2).[7] Similarly Ga introduces shallow acceptor levels at $E_v+0.317$ eV (h) and $E_v+0.333$ eV (k_1,k_2).[7] There is some indirect evidence of the existence of deep acceptor levels associated with Al (Refs. 4 and 8) but none for deep levels associated with Ga.

The shallow acceptors introduced in SiC by the group-III impurities have been studied using electron paramagnetic resonance (EPR),[9–16] Optically Detected Magnetic Resonance (ODMR),[16–20] high-frequency pulsed EPR and electron-nuclear double resonance (ENDOR) at 95 GHz,[21] and by ENDOR at conventional frequencies.[22,23] It appears that the behavior of the sB acceptor is strikingly different from that of the shallow Al (sAl) and shallow Ga (sGa) acceptors. The resonance conditions of the unpaired spin related to the sAl and sGa acceptors reflect the properties of the uppermost Γ_9 valence-band hole and indicate an effective-mass-like character of these acceptors but with reduced orbital-momentum contribution resulting from the localization. In contrast, the EPR spectrum of the sB acceptor did not show effective-mass-like behavior. The contribution of orbital angular momentum appears to be almost negligible ($g\sim 2$) and, for instance, EPR signals of sB could be observed in 3*C*-SiC without any uniaxial stress applied to the crystal in contrast to sAl and sGa in the same material.

The difference in behavior of sB, on the one hand, and sAl and sGa, on the other hand, was explained by considering the difference in atomic radii.[15,16,21] It was proposed that

B, which substitutes for Si but which has an atomic radius smaller than Si, occupies an off-center position owing to chemical rebonding, i.e., it relaxes away from the neighboring C along the B-C bond. Indeed a high-frequency (95 GHz) EPR and ENDOR study on sB in 6*H*-SiC revealed that there is a relaxation of the neighboring carbon atom and the boron atom away from each other.[21] This study also revealed that *B* is neutral and that it carries no direct spin density. The main spin density (about 40%) is located on the dangling bond p_z orbital of the neighboring carbon atom along the C-B connection line. In contrast to the behavior of the sB acceptor, Al and Ga atoms substituting for Si are expected to occupy on-center positions. As the local symmetry is conserved this could explain the effective-mass-like behavior observed for the sAl and sGa acceptors.

The first magnetic-resonance observation of dB acceptors in SiC was made using ODMR techniques.[19,20,24,25] The ODMR spectra were recorded by monitoring the intensity of the yellow luminescence band in 6*H*-SiC and its analogue in 4*H*-SiC. A number of anisotropic signals were observed at 1.5 K, which were ascribed to dB acceptors, and which originated from several types of centers since the relative intensities of the signals vary with the emission wavelength in the luminescence band. The most intense ODMR lines showed nearly axial symmetry around the hexagonal *c* axis and exhibited $g_{\parallel}=2.02-2.03$ and $g_{\perp}\approx 2.0$. The low resolution of the ODMR method did not allow the observation of B hyperfine (hf) structures to connect the spectra unambiguously with a B impurity. Subsequent EPR studies at 9.5 GHz on the dB acceptor in 6*H*-SiC showed the same *g* parameter as observed in the ODMR experiments[19] leading to the conclusion that in the optical experiments the same dB center is involved. Preliminary ENDOR measurements of dB revealed ^{11}B signals.[26] Later EPR spectra of dB were also observed in 4*H*-SiC and 3*C*-SiC.[27]

The features of the EPR spectra of dAl and dGa (Refs. 13–16) are almost identical to those observed for dB. Importantly, no effective-mass-like behavior was observed for these three deep acceptors. The orientational dependencies of the EPR spectra indicate that the deep centers of B, Al, and Ga have the same, nearly axial, symmetry around the hexagonal *c* axis in the hexagonal polytypes of SiC and around the ⟨111⟩ axis in 3*C*-SiC. The *g* values are such that $g_{\parallel}>2.0$ and $g_{\perp}\approx 2.0$ ($g_{\parallel}>g_{\perp}$ in contrast to sB).[13–16]

It was proposed[13–16] that the dB, dAl, and dGa acceptors consist of a group-III element on a Si position accompanied by a neighboring carbon vacancy (A_{Si}-V_{C}). It was argued that this center has near-axial symmetry around the *c* axis and that the hyperfine interaction with the B, Al, and Ga nuclei is of the same order of magnitude as for sB, sAl, sGa, which were established to be B_{Si}, Al_{Si}, and Ga_{Si} centers. It is interesting to note that in contrast to the shallow acceptors, which show a strong difference in behavior between sB, on the one hand, and sAl and sGa, on the other hand, the deep acceptors of these group-III elements show almost the same behavior.

The existence of deep B, Al, and Ga acceptors levels in addition to the shallow B, Al, and Ga centers is quite interesting and has also practical consequences with regard to the fabrication of SiC devices. For instance EPR spectra of deep Al could be easily detected in commercial Cree Corporation Al-doped *p*-type SiC substrates. However, the (A_{Si}-V_{C}) model for these deep acceptors is by no means firmly established and, for example, several questions regarding the experimental observations remained unanswered. To further support the idea that dB, dAl, and dGa acceptors do exist and that the proposed (A_{Si}-V_{C}) model may explain the observations, we have started an investigation of these centers using high-frequency (95 GHz) EPR and ENDOR techniques. The use of these high-frequency techniques was stimulated in particular by the success of a similar study on sB in 6*H*-SiC.[21] Here we present the results obtained on the dB acceptor. In particular, the hyperfine data obtained on ^{11}B, ^{13}C, and ^{29}Si nuclei supply support for the (A_{Si}-V_{C}) model proposed in previous publications. These hyperfine data have not only been obtained by pulsed ENDOR techniques at 95 GHz but also by modern electron spin echo envelope modulation (ESEEM) and hyperfine sublevel correlation (HYSCORE) spectroscopy techniques at 9.5 GHz.

II. EXPERIMENT

The 6*H*-SiC samples were free-standing epitaxial layers (with removed substrates) and Lely-grown crystals compensated with ^{11}B during diffusion (95–99% of the boron is ^{11}B). The epitaxial layers were grown by the sublimation sandwich method[28] in vacuum at temperatures between 1700 and 1750 °C. As grown, the epitaxial layers were *n*-type, owing to nitrogen donors. Boron was diffused at a temperature of about 2000 °C. Two types of samples were available: ^{13}C-enriched ($\sim$30%) crystals of 6*H*-SiC and crystals with a natural isotopic abundance ($\sim$1%) of ^{13}C.

The high-frequency EPR experiments were performed at 1.2 K on a home-built, pulsed EPR/ENDOR spectrometer operating at a microwave frequency of 95 GHz. A detailed description of the setup is given elsewhere.[29,30] The main advantage of this spectrometer is the high resolution both in the EPR and the ENDOR spectra. Moreover, owing to the split-coil configuration of the superconducting magnet, it is possible to perform a complete orientational study. The pulsed ESE-detected EPR spectra were measured by monitoring the electron spin-echo intensity in a two-pulse echo experiment as a function of the magnetic field [see Fig. 1(a)]. In the pulsed ENDOR experiment a Mims-type pulse sequence was used[31] consisting of three $\pi/2$ microwave pulses with separations τ and T between the first and the second, and between the second and third pulse, respectively [see Fig. 1(b)]. As a result of this pulse sequence a stimulated echo (SE) is created at a time τ after the last pulse. During the time T, which is much longer than the phase memory time T_M, a radio-frequency (RF) pulse is applied that induces a change in the intensity of the SE when this RF pulse is resonant with a nuclear transition.

The *X*-band (9.3 GHz) EPR experiments were performed at 1.2 K on a Bruker ESP380E Fourier transform-EPR spectrometer at 9.355 GHz.[32] To measure the EPR spectra again, a two-pulse scheme was used as shown in Fig. 1(a). In addition ESEEM experiments were performed. In these ESEEM experiments, the precession frequencies of the nuclear spins that are coupled to the unpaired electron spin appear as modulations of the electron spin-echo decay. The ESEEM measurement is performed using a two-pulse as well

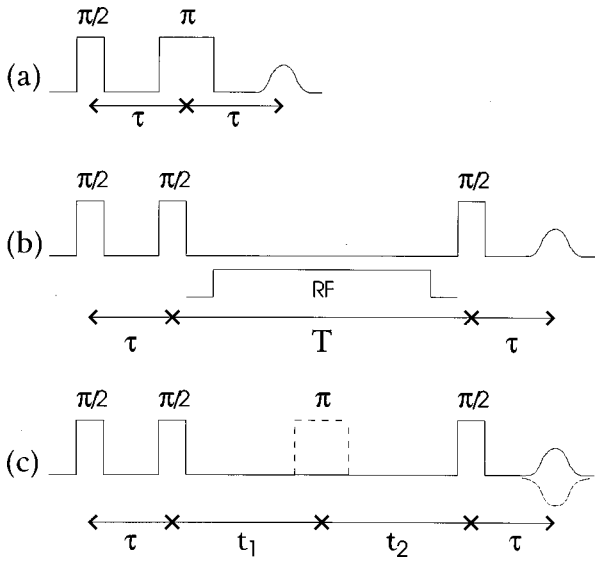

FIG. 1. The microwave pulse schemes in the two-pulse sequence (a), three-pulse sequence (b), and HYSCORE pulse sequence (c).

as a three-pulse sequence. In the first case the ESE intensity is recorded as a function of the time τ between the two microwave pulses. When using a three-pulse sequence the ESE intensity is recorded as a function of the time T between the second and the third $\pi/2$ microwave pulse. The frequency-domain ESEEM spectrum is obtained as a fast Fourier transform of the modulation patterns of the echo signal.

In the HYSCORE spectroscopy experiments a four-pulse sequence is applied [see Fig. 1(c)] consisting of three $\pi/2$ pulses and a π mixing pulse between the second and the third pulse. This mixing pulse creates correlations between the coherences of the nuclear-spin transitions associated with the two electron-spin m_s manifolds. The HYSCORE technique was introduced by P. Höfer *et al.*[33] In this two-dimensional experiment the ESE amplitude is recorded as a function of the time t_1 between the second and the third, as well as a function of the time t_2 between the third and the fourth pulse. The two-dimensional (2D) time-domain spectrum is then subjected to a fast Fourier transform with respect to t_1 and t_2 to create a two-dimensional spectrum in frequency space. The advantage of HYSCORE is that the correlation of the nuclear-spin coherences between the two electron-spin m_s manifolds shows up in the two-dimensional spectrum. In both the ESEEM and HYSCORE experiment the width of the $\pi/2$ pulse was adjusted to 16 ns, and the microwave power was then set for the maximum amplitude of the echo. The HYSCORE mixing pulse was optimized to 32 ns, resulting in an $\sim$80% inversion of the stimulated echo. For the three-pulse ESEEM experiment the time between the second and the third pulse was swept from 272 to 9872 ns in 600 steps of 16 ns. In the HYSCORE experiment the time between the first and the second pulse was 360 ns, the time between the second and the third pulse was swept from 272 to 4368 ns and between the third and the fourth from 288 to 4384 ns in 256 steps of 16 ns for both directions. To get rid of unwanted echoes eight-step phase cycling was used. The processing of the HYSCORE spectra was done using the Bruker WIN-EPR system program. First, the unmodulated T_1 relaxation decay was removed from the time-domain spectrum by subtracting a quadratic function, as this relaxation would give a dominating zero-frequency component in the fast Fourier transform (FFT) spectrum, obscuring the real hyperfine lines. Further processing steps included a Hamming apodization and zero filling in both dimensions. After 2D FFT, the magnitude spectrum was calculated and symmetrized.

III. RESULTS

The EPR, ENDOR, ESEEM, and HYSCORE spectra obtained on the dB acceptor can be described with a spin Hamiltonian of the following form:

$$H=\mu_B\vec{\mathbf{S}}\cdot\vec{\vec{g}}\cdot\vec{\mathbf{B}}+(\vec{\mathbf{S}}\cdot\vec{\vec{A}}_{\mathrm{B}}-\gamma_{\mathrm{B}}\vec{\mathbf{B}})\cdot\vec{\mathbf{I}}_{\mathrm{B}}+\mathbf{I}_{\mathrm{B}}\cdot\vec{\vec{P}}_{\mathrm{B}}\cdot\vec{\mathbf{I}}_{\mathrm{B}}+\sum_i(\vec{\mathbf{S}}\cdot\vec{\vec{A}}_X^i-\gamma_X\vec{\mathbf{B}})\cdot\vec{\mathbf{I}}_X^i, \quad (1)$$

where X represents Si or C, $\vec{\vec{A}}_B$ and $\vec{\vec{A}}_X^i$ represent the hyperfine tensors of the $^{11}\mathrm{B}(I=\frac{3}{2})$, $^{13}\mathrm{C}(I=\frac{1}{2})$, and $^{29}\mathrm{Si}(I=\frac{1}{2})$ nuclear spins, $\vec{\vec{P}}_{\mathrm{B}}$ the quadrupole tensor of the ^{11}B spins, and γ_B and γ_X the magnetogyric ratios for the B, C, and Si nuclei. Assuming that the boron hf and quadrupole tensors have axial symmetry along the c axis and defining the c axis as the z axis of the axis system, we can write for the quadrupole interaction $P_{\mathrm{B}}(I_Z^2-\frac{1}{3}I^2)$. Further $A_{\mathrm{B}_{zz}}=A_{\mathrm{B}_{\parallel}}=a_{\mathrm{B}}+2b_{\mathrm{B}}$, $A_{\mathrm{B}_{xx}}=A_{\mathrm{B}_{yy}}=A_{\mathrm{B}_{\perp}}=a_{\mathrm{B}}-b_{\mathrm{B}}$, $P_{\mathrm{B}}=\frac{3}{2}P_{\mathrm{B}_{zz}}=3q_{\mathrm{B}}$, and $P_{\mathrm{B}_{xx}}=P_{\mathrm{B}_{yy}}=-q_{\mathrm{B}}$. Here q_{B} can be written in terms of the field gradient as

$$q_B=\frac{eQ}{4I(2I-1)}V_{ZZ}, \quad (2)$$

where Q is the electric quadrupole moment of ^{11}B and V_{ZZ} the electric field gradient.

A. *W*-band (95 GHz) EPR spectra

In Fig. 2 two EPR spectra are shown, one measured at 95 GHz (W band), the other at 9.3 GHz (X band). In both cases the magnetic field pointed along the c axis and the temperature was 1.2 K. On the high-field side we see the signal from the shallow-boron (sB) acceptor as studied in Ref. 21. On the low-field side we see the EPR signal of the deep-boron (dB) acceptor, as established in Ref. 13. The W-band spectrum of the dB acceptor shows two lines with relative intensity 2:1. The intense line is a sum of the lines attributed to the two quasicubic sites (k_1 and k_2); the other one is ascribed to the crystal site with hexagonal (hex) symmetry. We note that this is in agreement with the EPR measurements on a $4H$-SiC: ^{11}B crystal sample where two lines of the dB acceptor with a relative intensity of 1:1 are seen. In this crystal, only two sites are present, one quasicubic and one hexagonal site. The remarkable aspect of the W-band EPR spectrum compared to that taken at X band is the resolution enhancement owing to the larger g tensor splitting at higher microwave frequencies. The distance of the dB EPR signal to $g_e=2.0023$ is about 10 times larger than in the X-band spectrum. The same holds for the width of the dB EPR spectrum; the linewidth of the individual lines in the W-band spectrum

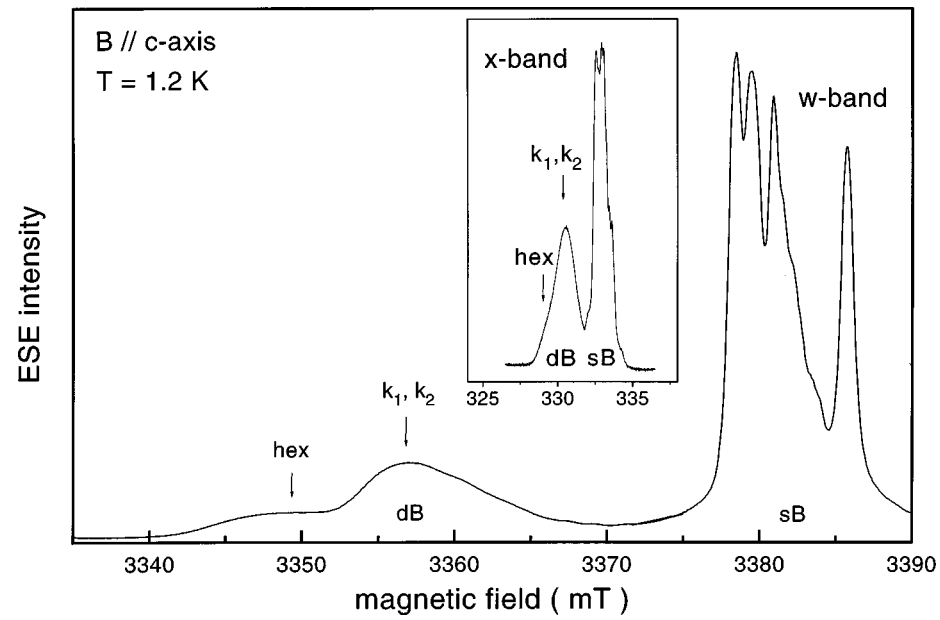

FIG. 2. Comparison between the EPR spectrum for $\mathbf{B}\|c$ of the deep and shallow ^{11}B acceptor at 95 GHz in 6H-Si ^{13}C and at 9.3 GHz in 6H-SiC (inset) at 1.2 K. The magnetic-field scale is the same for both spectra. The EPR signal, belonging to the deep (dB) and shallow (sB) acceptor center, respectively, is indicated. For the dB signal the parts of the EPR line of the hexagonal (hex) and quasicubic (k_1,k_2) site in the crystal are labeled as well.

is about 10 times broader than the width in the X-band spectrum. The intensity ratio between the dB and the sB signal is 1:2.2 at the X band and 1:6 at the W band. This fact indicates that the lines of the individual sites are much more spread in the W-band spectrum than in the X-band spectrum. The linewidth is much larger than can be attributed to T_2 and increases linearly with the microwave frequency, which suggests g strain.[39]

Figure 3(a) shows the orientational dependence of the dB acceptor EPR spectrum, with the magnetic field rotating in the $[11\bar{2}0]$ plane. This plane was determined using the known orientational dependence of the sB EPR spectrum.[21] The angle θ describes the orientation of the magnetic field with respect to the c axis. The angle φ describes the orientation of the magnetic field in a plane perpendicular to the c axis. For $\varphi=0°$ the magnetic field lies in the [1120] plane. From the figure it follows that the g tensor principal z axes of all three centers align with the c axis. This is contrary to the situation for the quasicubic sites of the sB acceptor, where the principal z axes of the g tensors lie along either

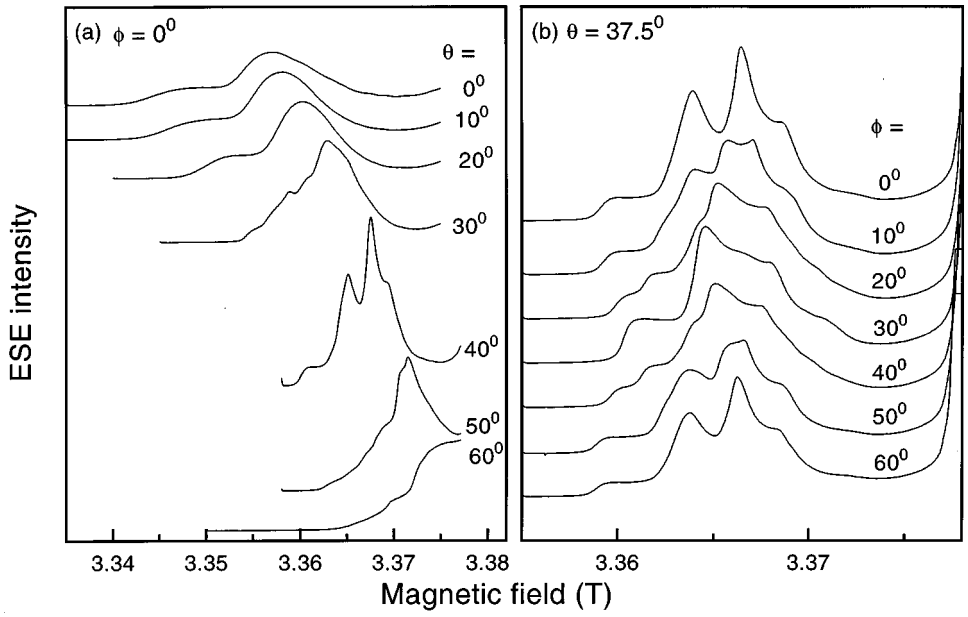

FIG. 3. Orientational dependence of the EPR spectrum of the deep ^{11}B acceptor at 95 GHz and 1.2 K in 6H-SiC. (a) Magnetic field rotating in the [1120] plane, where θ indicates the angle between the direction of $\mathbf{B}$ and the c axis. For angles $\theta>60°$ the dB EPR signal disappears underneath the sB EPR signal. (b) Dependence on φ, with the magnetic field describing a cone with $\theta=37.5°$. The slight nonaxiality of the g tensor is clearly visible.

TABLE I. g-tensor values for the deep boron (dB) acceptor from Ref. 13 and g tensor values as found at 95 GHz using the g value of the sB hexagonal site for $\mathbf{B}\|c$ as a g marker. The estimated difference between g_x and g_y for the hexagonal site is 0.01. For the k sites this value is expected to be smaller.

	$g_{\|}^{\text{hex}}$	$g_{\perp}^{\text{hex}}$	$g_{\|}^{k1}$	$g_{\perp}^{k1}$	$g_{\|}^{k2}$	$g_{\perp}^{k2}$	
dB	2.03	2.01	2.023	2.0	2.02	1.99	EPR (Ref. 13, 9.5 GHz, 4.5 K)
	2.027	2.01	2.022	2.01	2.021	2.00	EPR (95 GHz, 1.2 K)

one of the six other equivalent orientations in the hexagonal crystal lattice. The g tensor principal values, as found from the orientational dependence, are given in Table I. The values were determined using the sB hexagonal site EPR line at $\mathbf{B}\|c$ as a g marker. The g value of this line is 2.002 00, which was also used as a g marker in the case of the sB acceptor. In Fig. 3(b) we present the dependence of the EPR spectrum on φ for $\theta = 37.5°$. For this angle the slight g-tensor anisotropy of the six magnetically inequivalent sites in the plane perpendicular to the c axis is most clearly visible.

Similar experiments as presented in Figs. 2 and 3 were performed on a ^{13}C-enriched sample. No new EPR lines were observed in any orientation. Only a slight broadening of the EPR linewidth of the dB signals is seen which is attributed to the ^{13}C hyperfine interaction.

B. *W*-band ENDOR spectra

W-band ENDOR measurements were performed on nonenriched and 30% ^{13}C-enriched crystals. In Fig. 4 the spectra for $\mathbf{B}\|c$ are shown for both crystals, which show ENDOR transitions of ^{29}Si($I=\frac{1}{2}$), ^{13}C($I=\frac{1}{2}$), and ^{11}B($I=\frac{3}{2}$) nuclei. For clarity the spectrum around the silicon nuclear Zeeman frequency is magnified in an inset.

The ^{11}B ENDOR spectrum in Fig. 5 consists of three sharp lines and a broad hump, symmetrically located around the ^{11}B nuclear Zeeman frequency. As ^{11}B has a nuclear spin $I=\frac{3}{2}$ we expect three lines in each manifold for each site, due to the quadrupole interaction. The figure shows the magnetic-field dependence of the ^{11}B ENDOR lines as measured in the nonenriched sample. The three sharp lines vanish at low field (position 1), which corresponds to the hexagonal site. From this dependence we conclude that the three sharp lines belong to the quasicubic (qc) sites. We further see that the broad hump also consists of three lines and that they are related to the hex site. The ^{11}B hyperfine and quadrupole parameters derived from the ENDOR spectra are $|A_{\mathrm{B}_{\|}}^{\mathrm{qc}}| = 8.8$ MHz, $|A_{\mathrm{B}_{\|}}^{\mathrm{hex}}| = 5.4$ MHz, and $|P_{\mathrm{B}}^{\mathrm{qc}}| = |P_{\mathrm{B}}^{\mathrm{hex}}| = 190$ kHz, in agreement with the values reported by Baranov *et al.*[26] (see Table II a). Finally we mention that the ^{11}B ENDOR signals in the two $m_s=\frac{1}{2}$ and $m_s=-\frac{1}{2}$ manifolds have opposite sign. This phenomenon has now been observed several times in ENDOR experiments at 95 GHz and 1.2 K. It is explained by spin-lattice relaxation effects in the case of large thermal spin polarizations as it occurs at 95 GHz and 1.2 K. For a detailed explanation the reader is referred to a forthcoming paper.[34] Figure 6 shows the orientational dependence of the ^{11}B hyperfine lines of the lower manifold in the [1120] plane. The lines could not be followed further than 15° away from the c axis. Figure 6 also shows the orientational dependence of the ^{13}C line with the largest hyperfine interaction.

In Fig. 7 the ^{13}C ENDOR spectrum with $\mathbf{B}\|c$ is presented on an enlarged scale. It consists of a broad line around the ^{13}C nuclear Zeeman frequency and two separate lines at 32.2 and 40.0 MHz symmetrically positioned around the Zeeman frequency. The latter are probably due to the ^{13}C atoms with the highest spin density. The hyperfine constant $|A_{\mathrm{C}}^{\mathbf{B}\|c}| = 7.8$ MHz. In the broad line surrounding the ^{13}C Zeeman frequency several lines can be recognized with a maximum hyperfine value $|A_{\mathrm{C}}^{\mathbf{B}\|c}| = 2.2$ MHz.

The ^{29}Si ENDOR spectrum consists of a broad line at the ^{29}Si nuclear Zeeman frequency. Two lines can be distinguished with a hyperfine splitting $|A_{\mathrm{Si}}^{\mathbf{B}\|c}| = 0.76$ MHz.

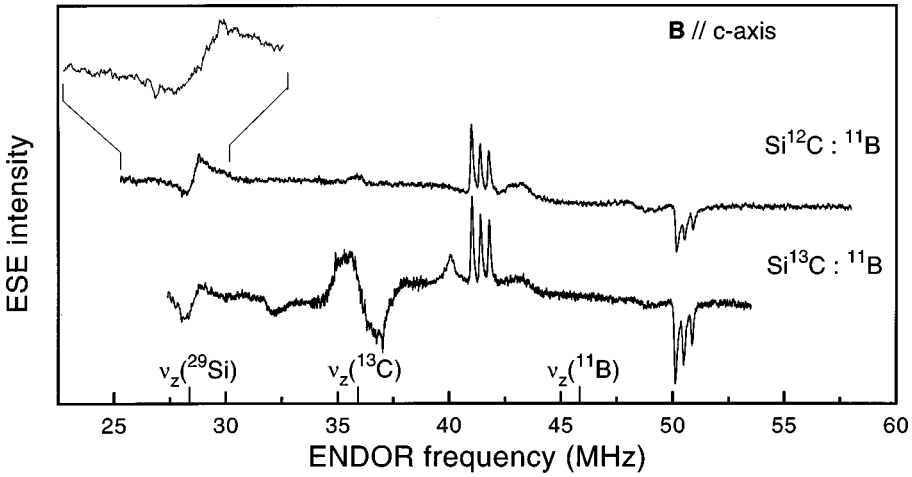

FIG. 4. Comparison between the ENDOR spectrum of the ^{13}C-enriched and the nonenriched sample at 95 GHz and 1.2 K. The part of the total spectrum that belongs to ^{11}B is magnified in Figs. 5 and 6. The lines belonging to ^{13}C are visible in the spectrum of the enriched sample and in Fig. 7 a magnification of this part of the total spectrum is shown. The spectrum around the ^{29}Si Zeeman frequency is magnified in an inset in this figure.

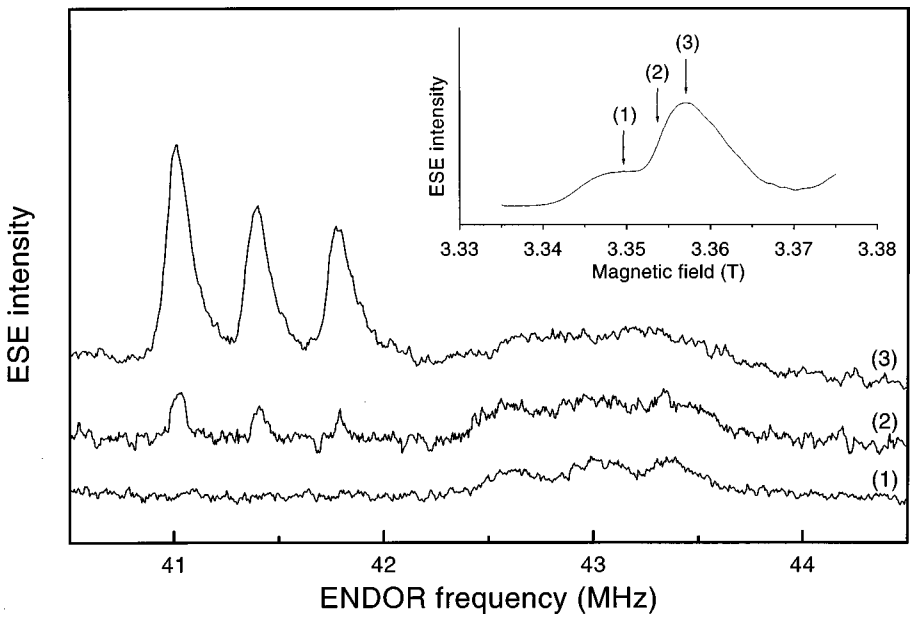

FIG. 5. Magnetic-field dependence of the ^{11}B ENDOR lines in the 6H-SiC sample for **B**$\|c$ axis at 95 GHz and 1.2 K. Spectrum (1) was measured with $B=3.349$ T, spectrum (2) with $B=3.353$ T, and spectrum (3) with $B=3.357$ T. From this figure it follows that the EPR line of the hexagonal site is much broader than the one of the quasicubic sites as the hf line of this site is always present in the spectra.

C. *X*-band three-pulse ESEEM and HYSCORE measurements on Si ^{12}C

As we note from the *W*-band ENDOR experiments presented in Fig. 4, the ^{11}B ENDOR transitions occur at frequencies that are shifted by about ± 4 MHz with respect to the ^{11}B nuclear Zeeman frequency at 46 MHz. By changing the EPR frequency from 95 GHz to 9.3 GHz the ^{11}B Zeeman frequency changes from 46 to 4.6 MHz and the ^{11}B ENDOR transitions are predicted to occur around 0–2 and 7–9 MHz. This is a very favorable situation to observe ESEEM spectra because for one m_s manifold the nuclear Zeeman frequency is then almost exactly canceled by the hyperfine interaction. As shown in Fig. 8(a) a deep nuclear modulation effect was observed in the stimulated echo decay at 9.3 GHz following a three $\pi/2$-pulse sequence by keeping τ fixed and varying the interval T between the second and the third $\pi/2$ pulse [see Fig. 1(b)]. In Fig. 8(b) the related frequency-domain spectrum is displayed as obtained by a FFT.

The attraction of the three-pulse ESEEM experiment is that there is no need to apply a RF field. It is, however, a one-dimensional technique with the inherent disadvantage that resonances of different nuclei in the same frequency

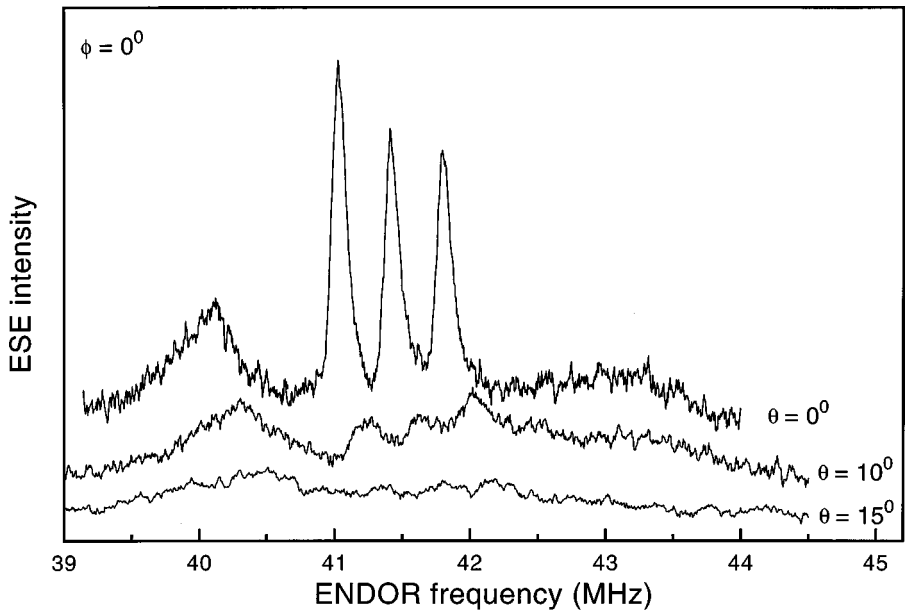

FIG. 6. Orientational dependence of the ^{11}B and the outer ^{13}C ENDOR line up to $\angle(B,c)=15°$ at 95 GHz and 1.2 K. The spectrum for $\theta=0°$ was measured at $B=3.357$ T, for $\theta=10°$ at $B=3.360$ T, and for $\theta=15°$, $B=3.361$ T. The lines are seen to broaden and the ^{13}C line splits into several lines. At angles $\theta>15°$, the lines have become too broad to be measurable by ENDOR spectroscopy.

TABLE II. (a) The experimental values of the hyperfine and quadrupole tensor of ^{11}B of the deep boron (dB) acceptor as found by ENDOR measurements at 95 and 9.5 GHz. (Definitions of the hyperfine and quadrupole parameters can be found in Ref. 42.) (b) The hyperfine parameters of ^{11}B for the shallow boron (sB) as well as the deep boron (dB) center as found from a fit of the orientational dependence of the ^{11}B hyperfine line in the ENDOR and HYSCORE spectra. The principal axes of the hf tensor coincide with the principal axes of the g tensor and a and b are related to the tensor elements of A as follows, $A_{\parallel}=a+2b$, $A_{\perp}=a-b$. In the paper about the sB acceptor by Matsumoto *et al.* (Ref. 21) the symbol q was used to describe the quadrupole constant. The relation between P and q is as follows, $P=3q=3/2\,P_{zz}$. (Definitions of the hyperfine and quadrupole parameters can be found in Ref. 42.)

(a)

	$A_{\parallel}^{hex}$	$A_{\perp}^{hex}$	P^{hex}	$A_{\parallel}^{k1}$	$A_{\perp}^{k1}$	P^{k1}	$A_{\parallel}^{k2}$	$A_{\perp}^{k2}$	P^{k2}	MHz
dB	5.4		0.19	8.8		0.19	8.9		0.19	ENDOR (95 GHz, 1.2 K)
	5.8		0.2	9.1		0.19	9.2		0.19	ENDOR (Ref. 13, 9.5 GHz, 4.5 K)

(b)

	a^{hex}	b^{hex}	P^{hex}	a^{k1}	b^{k1}	P^{k1}	a^{k2}	b^{k2}	P^{k2}	MHz
sB	-0.97	2.91	0.726	-3.72	3.06	0.765	-2.99	2.89	0.750	ENDOR (Ref. 23,
	±0.05	±0.05	±0.015	±0.05	±0.05	±0.015	±0.05	±0.05	±0.015	95 GHz, 1.2 K)
dB	2.6	1.7		3	3.1					HYSCORE (9.3
	±0.8	∓0.3		±1.5	∓0.9					GHz, 1.2 K)
	5.8			6.1	1.5		6.2	1.5		ENDOR (Ref. 13,
	±0.1			±0.1	∓0.1		±0.1	∓0.1		9.5 GHz, 4.5 K)

region form broad, unresolved lines from which it is difficult to extract the individual nuclear transitions. To disentangle these crowded spectra HYSCORE spectroscopy is the method of choice. In this technique a fourth π pulse is added to the three $\pi/2$-pulse sequence [see Fig. 1(c)] and the echo modulation patterns that are obtained are Fourier transformed with respect to t_1 and t_2. In this way a two-dimensional ENDOR spectrum is obtained. The function of the π pulse is to transfer coherences in one m_s manifold to the other one. The result is that off-diagonal resonances occur that correlate resonances of a particular nuclear spin in the two electron spin m_s manifolds. The attraction of such two-dimensional spectra is that it is relatively easy to separate nuclear transitions that otherwise overlap in a one-dimensional representation. In Fig. 9 we present as an example, a plot of the HYSCORE spectrum, obtained with the magnetic field tuned to the hexagonal EPR line in the spectrum with $\mathbf{B}\|c$, where the different peaks are indicated by their contour lines. Along the horizontal and vertical axis so-called ''skyline'' projections of the two-dimensional

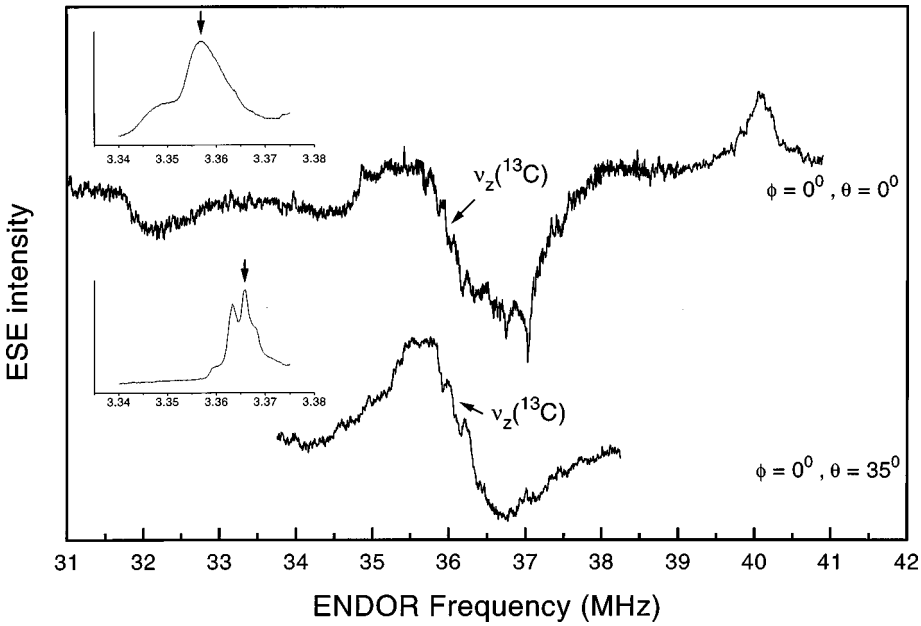

FIG. 7. The upper spectrum shows the ^{13}C ENDOR lines for $\mathbf{B}\|c$, with $B=3.357$ T (indicated by an arrow in the EPR spectrum in the upper inset) at 95 GHz and 1.2 K. The carbon Zeeman frequency, indicated by an arrow in the ENDOR spectrum, is 35.96 MHz at this field value. The largest hyperfine interaction visible is 7.8 MHz, all other interactions are smaller than 2.2 MHz. The lower spectrum shows the carbon ENDOR lines for the orientation $\varphi=0°$, $\theta=35°$, with $B=3.367$ T (indicated by an arrow in the EPR spectrum in the lower inset). The carbon Zeeman frequency, again indicated by an arrow in the ENDOR spectrum, is 36.04 MHz at this field value. The inner lines seem to have moved away from the carbon Zeeman frequency with respect to the upper spectrum.

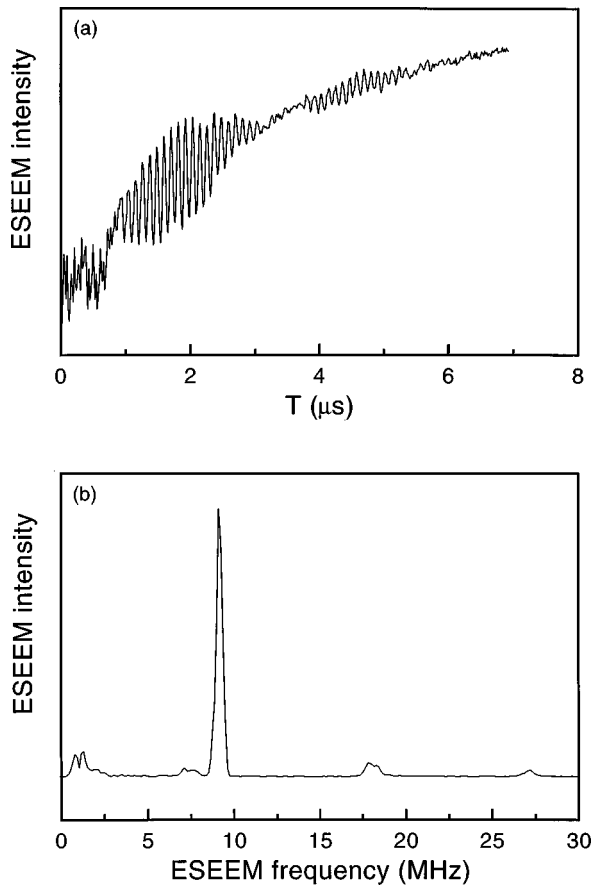

FIG. 8. (a) An example of an ESEEM spectrum in the time domain. (b) The spectrum of (a) after a fast Fourier transformation. The spectrum was measured on the quasicubic part of the EPR line. At 7.5 MHz we see the ^{11}B hf line belonging to the manifold above the ^{11}B nuclear Zeeman frequency of the hexagonal site. At 9 MHz we see the hf line of ^{11}B in the quasicubic site (consisting of three components, which are not visible in the picture), the line at 18 MHz is its second harmonic and the one at 27 MHz its third. The ^{11}B hf lines around 1 MHz belong to the manifold below the ^{11}B nuclear Zeeman frequency of the ^{11}B sites.

spectrum are given. It is seen that in these one-dimensional skyline projections the different transitions of the ^{13}C, ^{29}Si, and ^{11}B nuclei overlap and are difficult to disentangle. However in the two-dimensional plot the contributions of the different nuclei are easily distinguishable. The group of lines at the coordinates 2–7.5 MHz and 7.5–2 MHz belong to ^{11}B and the other groups to ^{29}Si as indicated in the figure. The clear separation in this two-dimensional plot of the resonances of the various nuclei allows us to follow the orientational dependencies of the ^{11}B resonances over a much larger range than in the one-dimensional ESEEM experiment at 9.3 GHz.

In Fig. 10 the orientational dependence of the ^{11}B hyperfine lines of the dB center are displayed, as obtained from the HYSCORE experiments, upon a rotation of the magnetic field in the [1120] plane. The squares and the circles present the angular dependence of the average value of the qc and hex hyperfine lines, respectively. As a comparison, the lines as expected at 9.355 GHz from the parameters found with ENDOR at *W* band are shown by filled diamonds. Assuming that the principal *z* axis of the hyperfine tensor of

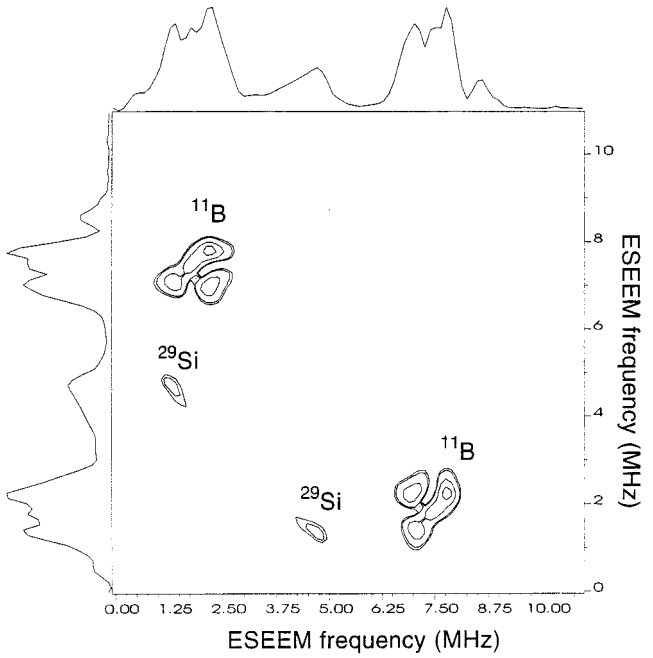

FIG. 9. A contour plot of the two-dimensional HYSCORE spectrum obtained on the hexagonal position in the EPR line with $\mathbf{B}\|c$ at 9.355 GHz and 1.2 K. In the figure we have indicated the lines belonging to ^{11}B and ^{29}Si. In the skyline projection the one-dimensional (1D) spectrum is recognized. The picture shows the advantage of 2D spectroscopy. One manifold of the ^{29}Si spectrum, which is not visible in the 1D projection appears well resolved in the 2D spectrum.

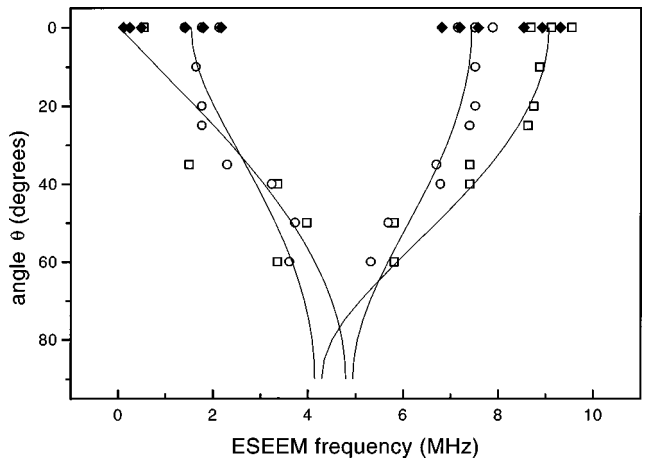

FIG. 10. Orientational dependence of the ^{11}B hyperfine lines in the [1120] plane at 9.355 GHz and 1.2 K. The squares show the hyperfine lines of the quasicubic site as measured by HYSCORE, the line through them was calculated using $a_B = 2.7$ MHz and $b_B = 3.2$ MHz. Estimating the error in these values leads to $a_B = 3 \pm 1.5$ MHz and $b_B = 3.1 \mp 0.9$ MHz. The circles show the hyperfine lines of the hexagonal site as measured by HYSCORE, the calculation parameters of the line are $a_B = 2.5$ MHz and $b_B = 1.7$ MHz. The estimated error is $a_B = 2.6 \pm 0.8$ MHz and $b_B = 1.7 \mp 0.6$ MHz. The black diamonds show the expected position of the lines at 9.355 GHz as derived from the experimental ENDOR data of 95 GHz and 1.2 K.

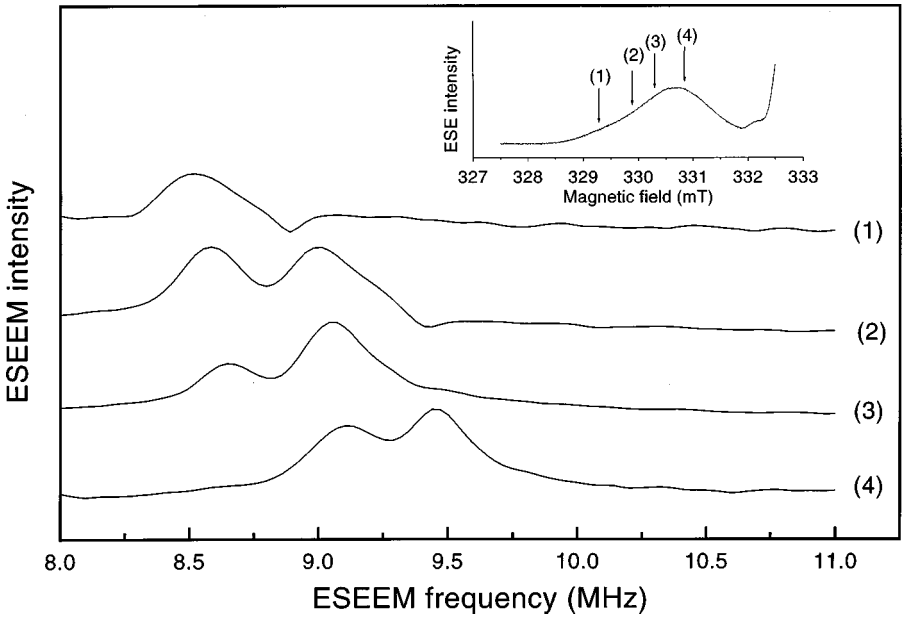

FIG. 11. Magnetic-field dependence of the three-pulse ESEEM lines at the high-frequency side of $\nu_z(^{11}\mathrm{B})$ for $\mathbf{B}\|c$ axis at 9.355 GHz and 1.2 K. Spectrum (1) was measured at $B=329.34$ mT, (2) at $B=329.95$ mT, (3) at B=330.37 mT, and (4) at $B=330.84$ mT. When the magnetic field is in position (1) in the EPR spectrum, we mainly connect the sublevels of the two m_s manifolds that have the largest energy difference. When the magnetic field is in position (4), we mainly connect the sublevels of the two m_s manifolds that have the smallest energy difference. As we can see in the picture, the nuclear transition at the lowest frequency is strongest for condition (1) and the one at the highest frequency for condition (4). Using this observation we find that the hf and quadrupole tensor have the same sign (Ref. 21).

^{11}B is along the c axis and that the tensor is axially symmetric, we can fit the angular dependencies to $\nu=a_\mathrm{B}+b_\mathrm{B}[3(\cos\theta)^2-1]$. We find that a_B and b_B must have the same sign and that $|a_\mathrm{B}^{\mathrm{hex}}|=2.6\pm0.8$ MHz, $|b_\mathrm{B}^{\mathrm{hex}}|=1.7\mp0.3$ MHz and $|a_\mathrm{B}^{\mathrm{qc}}|=3.0\pm1.5$ MHz, $|b_\mathrm{B}^{\mathrm{qc}}|=3.1\mp0.9$ MHz. As we could not measure the ESEEM spectrum for $\mathbf{B}\perp c$ axis, only $A_{\mathrm{B}_\|}$ is known accurately. The anisotropic hf parameter b_B thus has a large error margin, and so has a_B ($A_{\mathrm{B}_\|}=a_\mathrm{B}+2b_\mathrm{B}$). The quadrupole interaction is given by $P_{\mathrm{B}_\|}=190$ kHz for all sites. (See Table II b.)

We can derive the relative signs of the hyperfine and the quadrupole constants from a field-tagged hyperfine spectrum. In Fig. 11 we show the field dependence of the ^{11}B hyperfine lines, as obtained from the three-pulse ESEEM patterns with $\mathbf{B}\|c$, by varying the magnetic field over the EPR lines of the quasicubic site. When the ESEEM experiment is performed at the low magnetic-field side of the EPR line the ESEEM line at the lower frequency is strongest. When performing the experiment at the high magnetic field side the ESEEM line at the higher frequency is strongest. This fact indicates that the sign of the quadrupole interaction P_B of ^{11}B is the same as that of the hyperfine interaction A_B. This is in agreement with the conclusion of similar experiments on the sB acceptor.[21] As P_B is expected to be positive, as will be discussed in Sec. IV, we decide that $a_\mathrm{B}>0$, $b_\mathrm{B}>0$, and $P_\mathrm{B}>0$. The same effect can be seen in the ENDOR spectra published in Ref. 13.

D. T_2 measurements at 95 GHz

It appears that, with $\mathbf{B}\|c$, for the ^{13}C-enriched as well as for the nonenriched sample, the T_2 time is field dependent. As an illustration, we show in Fig. 12 the dependence of the EPR line shape on the interval τ between the microwave pulses in a two-pulse ESE experiment as measured on the ^{13}C-enriched sample. The EPR line intensity was normalized to unity to show the shift to higher magnetic field with increasing τ. The most important observation is that the T_2 time acquires its shortest value of about 0.8 μs for the largest deviation from $g=2$ (low magnetic-field side of the EPR line). On the high-field side of the EPR line the two-pulse echo decay exhibits a biexponential decay with time con-

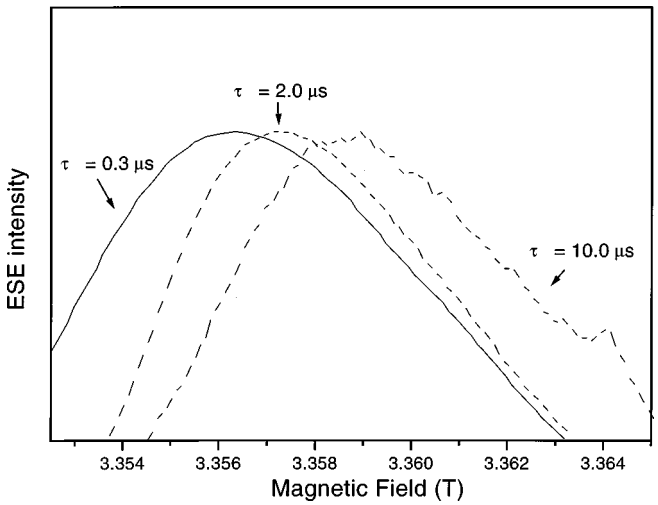

FIG. 12. The dependence of the shape of the EPR line on the time interval τ in a two-pulse ESE experiment with $\mathbf{B}\|c$ axis at 95 GHz and 1.2 K. Only the peak of the line of the quasicubic sites is shown to clearly demonstrate the shift of the line to higher field with increasing τ (spectra are normalized to unity). The peak at 3.364 T is due to Mn in the surface layer of the crystal.

stants of 4 and 17 μs. The field dependence of T_2 gradually decreases with increasing value of θ and disappears for angles $\theta > 35°$. Here a double exponential decay is observed with time constant $T_2^f \approx 2.5$ μs and $T_2^s \approx 14$ μs.

E. Nutation experiment at 95 GHz

In order to establish the spin multiplicity of the dB center we performed transient nutation measurements.[35] The sB center was taken as a reference because its spin quantum number is known to be $S=\frac{1}{2}$. If the spin multiplicity of the dB acceptor $S=1$, then the matrix element for the transition between the magnetic sublevels is $\sqrt{2}$ times larger than for $S=\frac{1}{2}$ and the length of the $\pi/2$ pulse should be shorter by this factor. If the spin multiplicity $S=\frac{3}{2}$ the transition moment between the $m_s=\pm\frac{1}{2}$ sublevels is even larger by a factor of 2 and the $\pi/2$-pulse length shorter by a factor of 2. We did find however that the length of the $\pi/2$ pulses for the sB and dB centers were equal and conclude that both centers correspond to $S=\frac{1}{2}$.

IV. DISCUSSION

The main results of our EPR, ENDOR, and ESEEM study on the deep boron acceptor in 6H-SiC can be summarized as follows. First of all, it was established that the spin multiplicity of our center is $S=\frac{1}{2}$. Second, we note that in contrast to the shallow boron acceptor the g tensors are almost axial with g_z parallel to the c axis for the hexagonal as well as for the quasicubic sites. The values of g_x, g_y, and g_z are such that $\Delta g_z=(g_z-g_e) \gg \Delta g_x=(g_x-g_e)$, $\Delta g_y=(g_y-g_e)$, and that $g_x \neq g_y$, i.e., there is a small nonaxiality. The EPR linewidth at 95 GHz is about ten times larger than at 9.3 GHz indicating a dominant g strain broadening that is most pronounced with $\mathbf{B} \| c$. Third, we note that the EPR spectrum in the ^{13}C-enriched sample does not exhibit ^{13}C hyperfine satellite lines, in contrast to the shallow boron acceptor. The maximum ^{13}C hyperfine interaction is estimated from the line broadening to amount to 3×10^{-4} T. In agreement with this finding is the fact that the ENDOR spectrum shows a maximum ^{13}C hf interaction of 7.8 MHz, which is equivalent to about 3×10^{-4} T. The fourth point of interest is that in the ENDOR spectrum no large ^{29}Si hyperfine interactions are observed. It is not excluded however, that one EPR line observed in the 9.3-GHz spectra for $\mathbf{B} \perp c$ on the high-field side of the shallow boron EPR line is a ^{29}Si hyperfine line with a hf splitting of about 40×10^{-4} T ($\sim 23\times10^{-4}$ T from the center of the sB signal). The fifth point is that the hf interaction and quadrupole interaction with ^{11}B is given by $a_B^{hex}=2.6\pm0.8$ MHz, $a_B^{qc}=3\pm1.5$ MHz, $b_B^{hex}=1.7\mp0.3$ MHz, $b_B^{qc}=3.1\mp0.9$ MHz, and $P_B=190$ kHz for all sites. The last point is that T_2 varies over the EPR line with $\mathbf{B} \| c$ and that T_2 is shorter on the low-field side of the EPR line, i.e., on the line belonging to the hexagonal site.

Following the ideas of Baranov and co-workers[13,26] we propose that the deep boron acceptor consists of a boron on a silicon position with an adjacent carbon vacancy. Apparently, for energetic reasons, this carbon vacancy combines always with a boron along the c axis. In Fig. 13 we show a simple one-electron linear combination of atomic orbitals (LCAO) molecular-orbital (MO) description of a carbon vacancy next to a boron substituting for a silicon atom.[36,37] The atomic orbitals are the dangling bonds of the three silicon atoms a, b, and c surrounding the vacancy. The point-group symmetry is C_{3v} and the totally symmetric orbital (a_1) is expected to be lowest with the degenerate orbital (e) lying above it. By populating these one-electron orbitals with the unpaired electron of the three silicons surrounding the vacancy, we see that one electron occupies the (e) orbital, thus explaining the $S=\frac{1}{2}$ character of the defect. Because of the orbital degeneracy a static Jahn-Teller distortion will take place, making one silicon atom inequivalent with respect to the other two and lowering the symmetry to C_{1h}. As a result the (e) orbital will split in an a' and an a'' component according to the two irreducible representations of C_{1h}. The one-electron LCAO MO's describing a' and a'' are $\lambda a + (\mu/\sqrt{2})(b+c)$ and $(\mu/\sqrt{2})(b-c)$. The observed directions of the principal axes and principal values of the g tensor are in agreement with this model. The g_z axis is found parallel to the vacancy-boron axis and the g_x axis is found in the [1120] plane. The value of g_z deviates most strongly from g_e because there is an expectation value of l_z (the z component of the orbital angular momentum operator) between the a' and a'' orbitals.[38] Since we are dealing with a hole this leads to a positive deviation of g_e.[36]

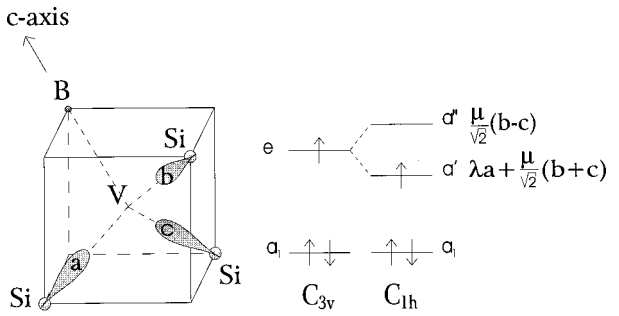

FIG. 13. Simple LCAO one-electron MO model for the electronic structure of the deep boron acceptor consisting of a boron substituting for a silicon and a neighboring carbon vacancy. In the description, we have followed the nomenclature of Watkins (Ref. 36). The B-V bond has the direction of the c axis [(111) direction in the cube]. a, b, and c are the three broken bonds of the Si atoms surrounding the vacancy. Without the Jahn-Teller distortion the point-group symmetry is C_{3v}, with the Jahn-Teller distortion the symmetry is C_{1h}. The one-electron LCAO MO's shown transform according to the irreducible representations of the symmetry group C_{1h}.

We propose that random g strain is the main reason for the linewidth observed at 95 GHz with $\mathbf{B} \| c$, because at 9.3 GHz the linewidth is about ten times smaller. This random strain in the crystal arises from a difference in local environments of the individual centers. The first EPR study that showed unambiguously the effect of random strain on the width of the EPR line was carried out by Feher, Hensel, and Gere[39] on the B acceptor in Si. In our case random g strain causes a spread in the energy difference between the a' and a'' orbital. Since this energy difference appears in the denominator of the expression for Δg, a spread in the orbital energies will thus lead to a spread in Δg. The reduction of the linewidth when the magnetic field is turned away from the c axis can also be understood because the contribution of

the spin-orbit coupling to Δg then reduces accordingly. Since the spin-orbit interactions involve the molecular orbitals of the center, the effective g values will be more sensitive to the local environment the further they are from g_e. The variation of T_2 over the EPR line with $\mathbf{B}\|c$ is not entirely clear. It could be caused by thermal modulation of the random strain which would give the largest variation in resonance frequencies (shortest T_2) for those centers that have a small difference in orbital energy (largest Δg). In this context it is interesting to note that Baranov and Mokhov[13] observed that the EPR line shifts to higher field when increasing the temperature. This effect can be explained by assuming that in the low-field part of the EPR line T_2 reduces faster with increasing temperature than in the high-field part.

From the ^{11}B hyperfine interaction data it is clear that there is a negligible spin density on boron. According to our model the anisotropic part of the hf interaction b_B is then determined by the dipole-dipole interaction between the unpaired electron spin in the three dangling bonds of the silicon atoms and the nuclear spin of ^{11}B. As the sign of b_B is determined by the factor $(3\cos^2\theta-1)$, with θ the angle between the c axis and the connection line from the nucleus to the spin density, b_B is expected to be positive. The symmetry axis of the hf tensor is expected to be parallel to the connection line between the boron and the vacancy, in agreement with the experimental data. To estimate the value of b_B we used a point-dipole approximation assuming sp^3 orbitals on the three silicons. To account for the unpaired electron spin we took fractional charges f $(-e)$ on the three Si atoms surrounding the vacancy. We placed 75% of the fractional charge at 0.77 Å from the silicon atoms on their connection lines with the vacancy and assumed 25% of the fractional electron spin to be located on the silicon nucleus. For a value of $f=30\%$ on one Si hybrid orbital this leads to $b_B=+1.1$ MHz. Using the observed values of b_B and comparing with the sB calculation we estimate the total spin density on the three silicons to be in the range of 70–90 %. The isotropic part of the boron hf interaction is very small and positive. Here we have to realize that only 0.1% of the spin density in the s orbital of boron gives $a_B\sim 3$ MHz. As in the case of shallow boron we do not think that there is a basis for a speculation on the value of a_B for boron.

The quadrupole tensor of ^{11}B is mainly determined by the electric-field gradient produced by the distribution of the three valence electrons in the orbitals of boron.[21] The value of P_B for ^{11}B with a sp^3 configuration with no electron present along the B-vacancy connection line is predicted to be positive and is estimated to amount to $P_B=1020$ kHz.[21] In the case of the sB acceptor the experimentally observed quadrupole constant P_B is 750 kHz, which is much larger than the value P_B of 190 kHz observed for the dB center. This difference may be explained by the fact that in the dB case the boron is less removed from its center position than in the case of the sB with an inherent smaller electric-field gradient. We note that Watkins[36] in his study of the Al-vacancy pair in Si also finds a surprisingly small quadrupole splitting of the ^{27}Al nucleus. This author devotes a long discussion to the possible explanations of this observation, one of them being a displacement of the Al towards the vacancy. The important point though is that P_B is predicted to be positive, which allows us to establish that the isotropic hf constant a_B and the anisotropic hf constant b_B are also positive. The fact that b_B is found to be positive is in agreement with the theoretical prediction for the sign of b_B (see above).

From the ENDOR spectrum of ^{13}C presented in Fig. 7 for $\mathbf{B}\|c$, it is seen that the largest hf interaction amounts to 7.8 MHz ($\sim 3\times10^{-4}$ T). Unfortunately, it was not possible to perform a reliable orientational study of the two outer ENDOR lines because the lines broaden quickly when turning the magnetic field away from the c axis. We attribute the lines to the nine ^{13}C atoms adjacent to the three Si atoms surrounding the vacancy. If we take the observed hf splitting of about 3×10^{-4} T as a measure for the isotropic hf constant a_C then a simple estimate[40] would yield 0.2% s character on each of the nine adjacent ^{13}C atoms. Assuming sp^3 hybrid orbitals the total spin density on the nine ^{13}C atoms adjacent to the silicons surrounding the vacancy is estimated to be about 7.2%. It is interesting to note that apart from the two ^{13}C ENDOR lines in Fig. 7 at ± 7.8 MHz away from $\nu_z(^{13}\mathrm{C})$, the other ^{13}C lines are grouped closely around $\nu_z(^{13}\mathrm{C})$. This indicates that the spin density is almost 100% localized on the three silicons surrounding the vacancy and the nine adjacent carbon atoms. In contrast, the ^{13}C ENDOR spectrum of the shallow boron acceptor exhibits a much more gradual distribution of the ENDOR lines[21] typical for a more shallow center where the spin density is distributed over a larger volume.

The proposed model for the deep boron acceptor would predict a large hf splitting of the ^{29}Si nuclei surrounding the vacancy, whereas in the ENDOR spectrum of Fig. 4 only ENDOR lines closely around $\nu_z(^{29}\mathrm{Si})$ are observed. A rough idea about the hf splitting expected for the ^{29}Si atoms surrounding the vacancy can be found from the splitting seen in the case of the sB acceptor for the carbon atom carrying the main spin density. This carbon carries 38% of the spin density and its hyperfine interaction is given by $a_C=(40.8\pm1)\times10^{-4}$ T and $b_C=(10.8\pm0.5)\times10^{-4}$ T. Assuming a spin density of 25–30 % on each of the three silicons, we expect their hyperfine interaction to be of the same order of magnitude. Itoh *et al.*[41] measured the hf interaction of the nearest-neighboring silicons of a positively charged carbon vacancy in Al-doped, 1 MeV electron-irradiated 3C-SiC to be $A_\parallel=-20.2\times10^{-4}$ T and $A_\perp=-14.8\times10^{-4}$ T. A satellite line on the high-field side of the shallow boron EPR transition is observed in the X-band spectrum, about 23×10^{-4} T separated from the center of the sB signal for $\mathbf{B}\perp c$. It exhibits the same temperature and orientational dependence as the main deep boron signal.[16] [In measurements on 3C-SiC at the X band a similar line was observed, with an extreme position at $\angle(\mathbf{B},c)\sim 70°$.][27] We tentatively ascribe this satellite line to the ^{29}Si surrounding the vacancy. Confirmation of this assignment has to wait for the preparation of ^{29}Si-enriched boron-doped crystals.

The spin-density distribution in the dB acceptor site is summarized with the help of Fig. 14. The Si nuclei are calculated to each carry a spin density of 25–30 % with an estimated isotropic hf interaction of $30-40\times10^{-4}$ T. The adjacent carbons ($C_{2\alpha}$,$C_{2\beta}$) each carry a spin density of about 0.8% assuming an isotropic hf interaction of 2.8×10^{-4} T (7.8 MHz). The next silicons $Si_{2\alpha}$ carry a spin

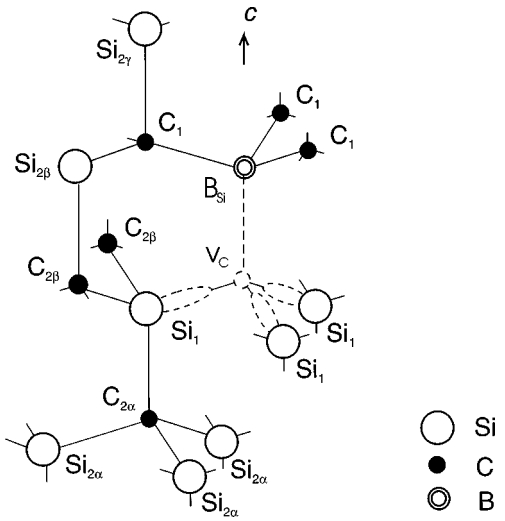

FIG. 14. The spin density distribution in the deep boron acceptor (hexagonal site). V_c indicates the position of the vacancy, substituting for carbon, B_{Si} indicates the position of the boron impurity substituting for silicon. On the ground of our ENDOR and HYSCORE data we suggest the following spin-density distribution. On the boron nucleus the spin density is negligible. About 25–30 % resides on each Si_1, about 0.2% on each $Si_{2\beta}$ and about 0.1% on each $Si_{2\alpha}$. The other Si have a negligible spin density. On each C_1 there is about 0.2% of spin density, on each $C_{2\alpha}$ and $C_{2\beta}$ about 0.8%. On the other carbons the spin density is negligible.

density $<0.1\%$ assuming an isotropic hf interaction of 0.3×10^{-4} T (0.76 MHz). The boron has a negligible spin density and the adjacent carbons (C_1) have a spin density of about 0.2% assuming an isotropic hf constant of 0.8×10^{-4} T (2.2 MHz). The next nearest silicons $Si_{2\beta}$ have a spin density of about 0.2% assuming an isotropic spin density 0.9×10^{-4} T (2.6 MHz). The others ($Si_{2\gamma}$) have an almost negligible spin density ($a_{Si}<0.3\times10^{-4}$ T).

Although the proposed model for the deep boron acceptor is consistent with the experimental observations, there are several alternative models that deserve consideration. In the first, we consider the situation that boron substitutes for a carbon atom with a neighboring vacancy on a silicon position. In this model the unpaired spin density would reside on the carbon surrounding the vacancy and a large ^{13}C hyperfine interaction in the EPR spectrum of the ^{13}C-enriched crystal is expected, in analogy to the case of the shallow boron acceptor.[21] As we mentioned, we only observe a slight broadening of the EPR lines in the ^{13}C-enriched crystal and for this reason we exclude this alternative. In the second model, we assume boron to substitute for a carbon without the presence of a vacancy but with an electron transferred from the back bonds of a neighboring silicon atom to the boron. The absence of a large ^{11}B hf interaction excludes this model. The third possibility is that the boron substitutes for a carbon, that there is no vacancy, and that the three back bonds of boron donate the electron. This model can also be ruled out because the 95-GHz ENDOR spectra reveal that the ^{11}B hf interactions are almost the same as those observed for the shallow boron acceptor. In the fourth model, boron is accompanied by an impurity atom. The most common impurity is nitrogen. However, experiments with *N* concentrations varying over three orders of magnitude show that the deep-boron acceptor EPR signal is not affected. Further, we note that the deep-boron acceptor signal is not sample dependent, which excludes oxygen or any transition metal impurity to be involved in the structure of the deep-boron acceptor. In the fifth model, a boron atom on a silicon site is accompanied by a silicon on a nearest-neighbor carbon site. In this model the unpaired spin density would be located in a dangling bond of the antisite silicon atom and a g_z value close to $g_e=2$ would be expected in contrast to our experiments.

Finally, it is interesting to discus our model for the dB acceptor in relation to the conclusion of Kuwabara and Yamada.[2] These authors showed that the donor-acceptor-pair (DAP) luminescence involving the dB acceptor and the *N* donors is of type I, meaning that the donor and acceptor occupy the same (carbon) sublattice. This conclusion is not necessarily in contradiction to our model because in the DAP luminescence, the final negatively charged state of the dB acceptor is involved, whereas in our experiments, the neutral charge state is observed. If the conclusion of Kuwabara and Yamada is correct, this would imply a reconstruction of the dB acceptor upon the adding of an electron to the neutral charge state of the complex. This is an interesting supposition which would deserve further (theoretical) investigation.

V. CONCLUSION

The pulsed EPR and ENDOR results at 95 GHz and 9.3 GHz lend support to the model for the deep boron acceptor in which a boron in a silicon position combines with a neighboring carbon vacancy along the hexagonal *c* axis. A reasonable estimate of the spin-density distribution is obtained. It is shown that the spin density is distributed over a smaller volume than in the case of the shallow boron acceptor. The results demonstrate the power of pulsed ENDOR spectroscopy. In particular the ESEEM and HYSCORE experiments at 9.3 GHz allow us to resolve the angular dependence of the ^{11}B hf interaction with a precision that cannot be obtained with conventional ENDOR techniques. These HYSCORE results on ^{11}B turn out to be important for the interpretation of the electronic structure of the deep boron acceptor.

ACKNOWLEDGMENTS

This work forms part of the research program of the Stichting voor Fundamenteel Onderzoek der Materie (FOM) with financial support from the Nederlandse Organisatie voor Wetenschappelijk Onderzoek (NWO). Further support was obtained from the Human Capital and Mobility (HCM) program of the Commission of the European Community under Contracts Nos. ERBCHRXCT93028 and ERBCIPDCT940612. P.G.B. thanks the financial support given by NWO under Grant No. 047.005.12.96. T.I. thanks the financial support from JSPS.

[1] G. Pensl and R. Helbig, Festkoerperprobleme **30**, 133 (1990), and references therein.
[2] H. Kuwabara and S. Yamada, Phys. Status Solidi A **30**, 739 (1975).
[3] M. Ikeda, H. Matsunami, and T. Tanaka, Phys. Rev. B **22**, 2842 (1980).
[4] M. M. Anikin, A. A. Lebedev, A. L. Syrkin, and A. V. Suvorov, Fiz. Tekh. Poluprovodn. **19**, 114 (1985) [Sov. Phys. Semicond. **19**, 69 (1985)].
[5] W. Suttrop, G. Pensl, and P. Laning, Appl. Phys. A: Solids Surf. **51**, 231 (1990).
[6] V. S. Ballandovich and E. N. Mokhov, Semiconductors **29**, 187 (1995).
[7] M. Ikeda, H. Matsunami, and T. Tanaka, J. Lumin. **20**, 111 (1979).
[8] G. C. Rybicki, J. Appl. Phys. **78**, 2996 (1995), and references therein.
[9] H. H. Woodbury and G. W. Ludwig, Phys. Rev. **124**, 1083 (1961).
[10] A. G. Zubatov, I. M. Zaritskii, S. N. Lukin, E. N. Mokhov, and V. G. Stepanov, Fiz. Tverd. Tela Leningrad **27**, 322 (1985) [Sov. Phys. Solid State **27**, 197 (1985)].
[11] K. Maier, J. Schneider, W. Wilkening, S. Leibenzeder, and R. Stein, Mater. Sci. Eng. B **11**, 27 (1992).
[12] N. P. Baran, V. Ya. Bratus, A. A. Bugai, V. S. Vikhnin, A. A. Klimov, V. M. Maksimenko, T. L. Petrenko, and V. V. Romanenko, Phys. Solid State **35**, 1544 (1993), and references therein.
[13] P. G. Baranov and E. N. Mokhov, Semicond. Sci. Technol. **11**, 489 (1996).
[14] P. G. Baranov and E. N. Mokhov, Fiz. Tverd. Tela Leningrad **38**, 1446 (1996) [Sov. Phys. Solid State **38**, 5 (1996)].
[15] P. G. Baranov, I. V. Ilyin, and E. N. Mokhov, Solid State Commun. **100**, 371 (1996).
[16] P. G. Baranov, Defect Diffus. Forum **148–149**, 129 (1997).
[17] K. M. Lee, Le Si Dang, G. D. Watkins, and W. J. Choyke, Phys. Rev. Lett. **45**, 390 (1980).
[18] P. G. Baranov, V. A. Vetrov, N. G. Romanov, and V. I. Sokolov, Fiz. Tverd. Tela Leningrad **27**, 3459 (1985) [Sov. Phys. Solid State **27**, 2085 (1985)].
[19] P. G. Baranov and N. G. Romanov, Appl. Magn. Reson. **2**, 361 (1991).
[20] P. G. Baranov and N. G. Romanov, Mater. Sci. Forum **83–87**, 1207 (1992).
[21] T. Matsumoto, O. G. Poluektov, J. Schmidt, E. N. Mokhov, and P. G. Baranov, Phys. Rev. B **55**, 2219 (1997).
[22] T. L. Petrenko, V. V. Teslenko, and E. N. Mokhov, Fiz. Tekh. Poluprovodn. **26**, 1556 (1992) [Sov. Phys. Semicond. **26**, 874 (1992)].
[23] R. Muller, M. Feege, S. Greulich-Weber, and J.-M. Spaeth, Semicond. Sci. Technol. **8**, 1377 (1993).
[24] N. G. Romanov, V. A. Vetrov, P. G. Baranov, E. N. Mokhov, and V. G. Oding, Pisma Zh. Tekh. Fiz. **11**, 1168 (1985) [Sov. Tech. Phys. Lett. **11**, 483 (1985)].
[25] P. G. Baranov, N. G. Romanov, V. A. Vetrov, and V. G. Oding, *Proceedings of the 20th International Conference on the Physics of Semiconductors* (World Scientific, Singapore, 1990), p. 1855.
[26] P. G. Baranov, E. N. Mokhov, A. Hofstaetter, and A. Scharmann, Pisma Zh. Eksp. Teor. Fiz. **63**, 803 (1996) [JETP Lett. **63**, 848 (1996)].
[27] P. G. Baranov, I. V. Ilyin, E. N. Mokhov, Fiz. Tverd. Tela (St. Petersbury) (to be published). [Phys. Solid State (to be published)].
[28] Yu. A. Vodakov, E. N. Mokhov, M. G. Ramm, and A. D. Roenkov, Krist. Tech. **5**, 729 (1979).
[29] R. T. Weber, J. A. J. M. Disselhorst, L. J. Prevo, J. Schmidt, and W. Th. Wenckebach, J. Magn. Reson. **81**, 129 (1989).
[30] J. A. J. M. Disselhorst, H. van der Meer, O. G. Poluektov, and J. Schmidt, J. Magn. Reson. **115**, 183 (1995).
[31] W. B. Mims, *Electron Paramagnetic Resonance* (Plenum, New York, 1992).
[32] K. Holczer, D. Schmalbein, and P. Barker, Bruker Rep. **1**, 4 (1988).
[33] P. Höfer, A. Grupp, H. Neberfur, and M. Mehring, Chem. Phys. Lett. **132**, 279 (1986).
[34] M. T. Bennebroek and J. Schmidt, J. Magn. Reson. (to be published).
[35] J. Isoya, H. Kanda, J. R. Norris, J. Tang, and M. K. Bowman, Phys. Rev. B **41**, 3905 (1990).
[36] G. D. Watkins, Phys. Rev. **155**, 802 (1967).
[37] M. Tinkham, *Group Theory and Quantum Mechanics* (McGraw-Hill, New York, 1964).
[38] N. M. Atherton, *Principles of Electron Spin Resonance* (Ellis Horwood, Chichester, 1993), Chap. 4.
[39] G. Feher, J. C. Hensel, and E. A. Gere, Phys. Rev. Lett. **5**, 309 (1960).
[40] J. R. Morton and K. F. Preston, J. Magn. Reson. **30**, 377 (1978).
[41] H. Itoh, M. Yoshikava, I. Nashiyama, S. Misawa, H. Okumura, and S. Yoshida, in *5th SiC and Related Materials Conference, Washington, DC, 1993*, edited by editors, IOP Conf. Proc. No. 137 (Institute of Physics, London, 1994), Chap. 3, pp. 255–258.
[42] N. M. Atherton, *Principles of Electron Spin Resonance* (Ellis Horwood, Chichester, 1993), Chaps. 3, 5, and 7.